

## Accepted Manuscript

Title: Mass-resolved ion microscope imaging over expanded mass ranges using double-field post-extraction differential acceleration

Author: Ang Guo Michael Burt Mark Brouard

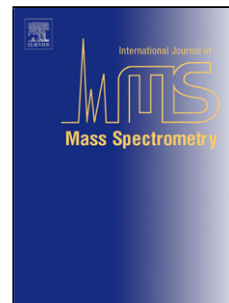
PII: S1387-3806(17)30074-X  
DOI: <http://dx.doi.org/doi:10.1016/j.ijms.2017.06.010>  
Reference: MASPEC 15819

To appear in: *International Journal of Mass Spectrometry*

Received date: 15-2-2017  
Revised date: 8-6-2017  
Accepted date: 22-6-2017

Please cite this article as: Ang Guo, Michael Burt, Mark Brouard, Mass-resolved ion microscope imaging over expanded mass ranges using double-field post-extraction differential acceleration, *International Journal of Mass Spectrometry* (2017), <http://dx.doi.org/10.1016/j.ijms.2017.06.010>

This is a PDF file of an unedited manuscript that has been accepted for publication. As a service to our customers we are providing this early version of the manuscript. The manuscript will undergo copyediting, typesetting, and review of the resulting proof before it is published in its final form. Please note that during the production process errors may be discovered which could affect the content, and all legal disclaimers that apply to the journal pertain.



# Mass-resolved ion microscope imaging over expanded mass ranges using double-field post-extraction differential acceleration

Ang Guo, Michael Burt, Mark Brouard\*

*The Department of Chemistry, University of Oxford, The Chemistry Research Laboratory, 12 Mansfield Road, Oxford, OX1 3TA, United Kingdom*

## Abstract

A modified post-extraction differential acceleration (PEDA) technique employing two pulsed electrodes was used to demonstrate mass-resolved stigmatic imaging over a broad  $m/z$  range. By varying the pulse voltages, a potential energy cusp was introduced into the ion acceleration region of an imaging mass spectrometer, creating two  $m/z$  foci that were tuned to overlap at the detector plane. This resulted in two focused  $m/z$  distributions that stretched the mass-resolved window with  $m/\Delta m \geq 1000$  to 165 Da without any loss in image quality; a range that doubled the 65 Da achieved under similar conditions using the original PEDA technique.

**Keywords:** Mass spectrometry imaging, post extraction differential acceleration (PEDA), spatial-map imaging, ion optics

## 1. Introduction

Mass spectrometry imaging (MSI) is widely used to obtain mass-specific surface images with micron or sub-micron spatial resolutions [1, 2, 3, 4]. Since its maturation in the late 1990's, MSI has frequently been coupled with matrix-assisted laser desorption ionization (MALDI) [5], secondary ion mass spectrometry (SIMS) [6], and desorption electrospray ionization (DESI) [7] to generate and image ions from a wide range of samples. This has led to its uptake in omics-based life sciences, where it has been applied to image polymers, metabolites, and other biomarkers [8, 9, 10, 11, 12, 13].

Imaging mass spectrometers are typically microprobe instruments where a focused laser, ion beam, or electrospray source is used to desorb and ionize molecules at a surface spot. Mass spectra are recorded with their locations by raster scanning the ionizing probe across the surface, enabling ion images to be reconstructed by plotting the intensity of specific ions at different probe positions. Like other scanning imaging techniques, such as electron microscopy [14], the spatial resolution of MSI is determined by the probe spot size. The drawback of this approach is that the time required to collect an image is inversely proportional to the area of the probe beam.

Microscope MSI has the potential to record spatially-resolved ion images faster than microprobe methods. In this approach, sample surfaces are illuminated with a defocused laser or ion beam, enabling all surface molecules to be desorbed and ionized simultaneously [15, 16, 17]. The spatial distribution of ions is then electrostatically projected onto a position-sensitive imaging detector at the end of a time-of-flight mass analyzer. This process is analogous to stigmatic microscopy, and has the advantage of decoupling spatial resolution from the probe beam size while retaining resolutions of 1-20  $\mu\text{m}$ .

Although the principles of ion microscopy have been well established since the 1960's [18], their uptake compared to microprobe instruments has been limited due to the difficulty in imaging more than one  $m/z$  (or range of  $m/z$ ) during an experimental cycle. The advent of event-triggered sensors, such as CMOS-based cameras [19, 20, 21], has overcome this problem by removing the need to apply time gates to the detector; ion images can now be recorded for every resolved  $m/z$  in a defined mass range during a single experiment [22, 23, 24].

The challenge in microscope MSI has therefore shifted from multi-mass imaging to the simultaneous optimization of mass and spatial resolution over a broad mass range. These are limited by the initial distribution of ion velocities at the sample surface. Mass resolution can be corrected using delayed extraction [25, 26, 27, 28], but the spatial resolution will remain poor as nothing prevents ions from diffusing away from their initial time-of-flight axes. Aoki and coworkers resolved this by developing the post extraction differential acceleration (PEDA) method [29], which extracts ions from a surface immediately following ionization to preserve their spatial resolution. Initial velocity distributions are then corrected by raising the potential of the extraction electrode after the ion packet has passed it. This causes slower ions of a particular  $m/z$  to accumulate more kinetic energy than quicker ions, creating a temporal focal point that is tuned to correspond with the detector plane. Using this approach, mass and spatial resolutions of 1450  $m/\Delta m$  and 4.0-5.5  $\mu\text{m}$  were simultaneously achieved. PEDA has since been applied over wide mass ranges using velocity corrected ion extraction [30], where the applied extraction field is retuned to shift the PEDA window to different  $m/z$  ranges without changing the image magnification or the mass and spatial resolutions.

This report describes an improved PEDA variant that uses an additional electrode to broaden the resolved mass window. The following sections introduce this 'double-field' PEDA concept, and experimentally compare it with the single-field method.

\*mark.brouard@chem.ox.ac.uk

## 2. Theory and simulations

In single-field PEDAs, lighter ions have earlier temporal focal points than heavier ions. As the field free drift length is fixed, ion optical voltages must therefore be tuned to focus a particular  $m/z$ , and the effective mass range is consequently centered around this focal point. The temporal foci of two  $m/z$  can be made to overlap by introducing a second pulsed electrode to the PEDAs acceleration region. This double-field PEDAs method is illustrated in Figure 1, where an additional electrode is inserted midway between the extractor and einzel lens entrance. The raised potentials of the two pulsed electrodes are used to create a cusp in the potential surface that divides the acceleration region in two. When the pulse applied to the new plate is less than half of that applied to the extractor, heavier ions in the ‘early’ acceleration region accelerate faster than lighter ions in the ‘late’ region. By adjusting the potential energy gradient on each side of the added electrode, an  $m/z$  from each segment of the acceleration region can be simultaneously focused, thereby broadening the achievable mass range. In the present work, the position of the added electrode and its applied pulse voltage are used to establish, at minimum, a 1000  $m/\Delta m$  resolution over the mass range between the two focused  $m/z$ . As these foci are governed by the electric fields in the ‘early’ and ‘late’ acceleration regions, it should be noted that the same effect can in principle be duplicated by repositioning the PEDAs electrode within the acceleration region and modifying the pulse voltage.

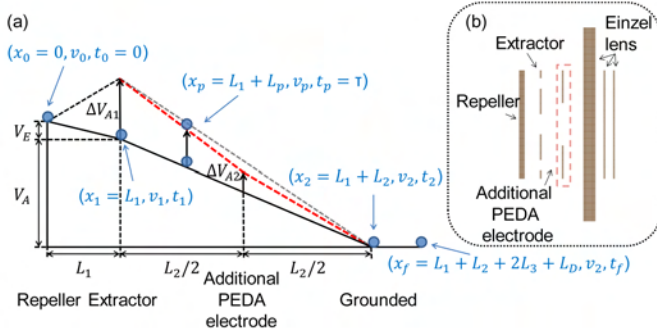


Figure 1: (a) The electrode potential energy surface (black line) before and after the application of single-field (black dashed line) and double-field PEDAs (red dashed line). In the double-field case, heavier ions in the ‘early’ acceleration region ( $L_1$  to  $L_1 + L_2/2$ ) accelerate faster than lighter ions in the ‘late’ region ( $L_1 + L_2/2$  to  $L_1 + L_2$ ), creating two focal points that are tuned to overlap at the detector. (b) The instrument ion optics used for single- and double-field PEDAs.

Following Aoki and coworkers, the extraction region in Figure 1 is defined with length  $L_1$  and potential difference  $V_E$  [29]. An ion with mass  $m$ , charge  $q$ , and initial velocity  $v_0$  extracted from the charged surface at  $x = 0$  will therefore accelerate to  $v_1$  when it reaches the extractor electrode at  $x = L_1$ . The flight time over this region is described by  $t_1$ .

$$v_1 = \sqrt{\frac{2}{m}(\frac{mv_0^2}{2} + qV_E)} \quad (1)$$

$$t_1 = \frac{mv_0 L_1}{qV_E}(-1 + \sqrt{1 + \frac{2qV_E}{mv_0^2}}) \quad (2)$$

The ion then enters an acceleration region between the extractor electrode and einzel lens entrance with potential difference  $V_A$  and length  $L_2$ . The additional PEDAs electrode is placed at  $x = L_1 + L_2/2$  with potential  $V_A/2$ . At a set time  $\tau$ , the extractor and PEDAs electrodes are raised by  $\Delta V_{A1}$  and  $\Delta V_{A2}$ , respectively. When these pulses are applied, the ion is located at  $x = L_1 + L_p$  with a velocity  $v_p$ . These are given by:

$$L_p = v_1(\tau - t_1) + \frac{qV_A}{2mL_2}(\tau - t_1)^2 \quad (3)$$

$$v_p = \sqrt{\frac{2}{m}(\frac{1}{2}mv_0^2 + q(V_E + V_A \frac{L_p}{L_2}))} \quad (4)$$

At  $\tau$ , ions located in the ‘early’ and ‘late’ acceleration region will accelerate differently. For ions at  $L_p \geq L_2/2$ , the potential increase resulting from the pulsed electrodes is the same as in the original PEDAs case.

$$\Delta V = 2\Delta V_{A2}(1 - \frac{L_p}{L_2}) \quad (5)$$

The potential change for ions at  $L_p < L_2/2$  is similar to the above, but accounts for the difference between  $\Delta V_{A1}$  and  $\Delta V_{A2}$ .

$$\Delta V = \Delta V_{A2} + (\Delta V_{A1} - \Delta V_{A2})(1 - \frac{L_p}{L_2/2}) \quad (6)$$

In both cases, the velocity of the ion as it leaves the acceleration region,  $v_2$ , is given by substituting the appropriate  $\Delta V$  into the following equation:

$$v_2 = \sqrt{\frac{2}{m}[\frac{mv_0^2}{2} + q(V_E + V_A + \Delta V)]} \quad (7)$$

The time at which the ion leaves the acceleration region also depends on its position. When  $L_p \geq L_2/2$ , the ion flight time at the einzel lens entrance,  $t_2$ , is:

$$t_2 = \tau + \frac{mv_p}{qE_2}[-1 + \sqrt{1 + \frac{qE_2(L_2 - L_p)}{mv_p^2/2}}] \quad (8)$$

To calculate  $t_2$  when  $L_p < L_2/2$ , the ion velocity and time-of-flight at the additional PEDAs electrode,  $v_m$  and  $t_m$ , must be determined. In the following,  $E_1$  and  $E_2$  are the electric field strengths of the ‘early’ and ‘late’ acceleration region, and are defined as  $\{2(\Delta V_{A1} - \Delta V_{A2}) + V_A\}/L_2$  and  $(2\Delta V_{A2} + V_A)/L_2$ .

$$t_2 = t_m + \frac{mv_m}{qE_2}(-1 + \sqrt{1 + \frac{qE_2 L_2}{mv_m^2}}) \quad (9)$$

$$v_m = \sqrt{\frac{2}{m}(\frac{1}{2}mv_p^2 + qE_1(L_2/2 - L_p))} \quad (10)$$

$$t_m = \tau + \frac{mv_p}{qE_1}(-1 + \sqrt{1 + \frac{qE_1(L_2/2 - L_p)}{mv_p^2/2}}) \quad (11)$$

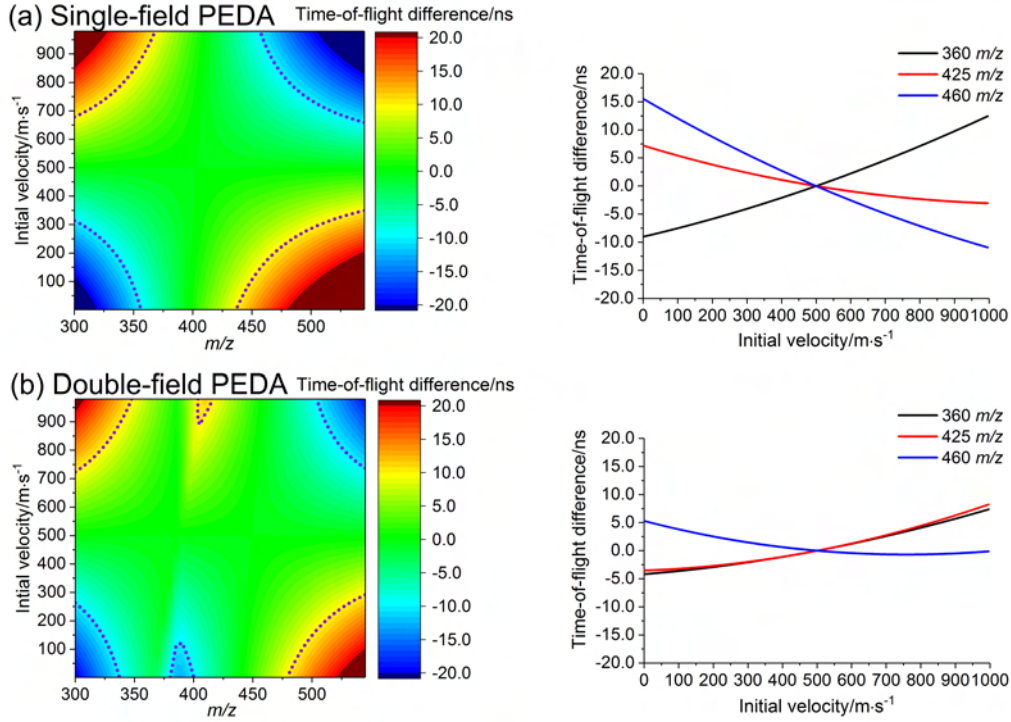


Figure 2: The calculated time-of-flight difference ( $t_d = t_f(v_0, \frac{m}{z}) - t_f(500 \text{ ms}^{-1}, \frac{m}{z})$ ) as a function of  $m/z$  and initial velocity  $v_0$  for (a) single-field PEDA and (b) double-field PEDA.

At this stage, the ion enters a conventional three-electrode einzel lens with a grounded entrance and exit. Each lens electrode is separated by a length  $L_3$ . The ion leaves the einzel lens at time  $t_3$  with the same velocity as it entered with, and passes through a field-free drift region of length  $L_D$  before impacting the detector. Its total time-of-flight,  $t_f$ , is therefore:

$$t_3 = t_2 + 2 \frac{v_2 m L_3}{q V_{lens}} \left( 1 + \sqrt{\frac{1 - 2qV_{lens}}{mv_2^2}} \right) \quad (12)$$

$$t_f = t_3 + \frac{L_D}{v_2} \quad (13)$$

As the electrode voltages ( $V_{repeller} = V_E + V_A$ ,  $V_{extractor} = V_A$ ,  $V_{PEDA1} = \Delta V_{A1} + V_A$ ,  $V_{PEDA2} = \Delta V_{A2} + V_A/2$ , and  $V_{einzel}$ ), the voltage switch time  $\tau$ , and the instrument lengths ( $L_1$ ,  $L_2$ ,  $L_3$ , and  $L_D$ ) are fixed, the time-of-flight of a particular ion reduces to a function of its initial velocity  $v_0$  and its mass to charge ratio  $m/z$ . The performance of the double-field PEDA method can therefore be assessed for a specific  $m/z$  by calculating its time-of-flight difference  $t_d$  about a mean  $v_0$ .

$$t_d = t_f(v_0, \frac{m}{z}) - t_f(500 \text{ ms}^{-1}, \frac{m}{z}) \quad (14)$$

In these calculations, the initial ion velocities are estimated to be normally distributed as  $v_0 = 500 \pm 500 \text{ ms}^{-1}$  based on previous reports [31, 32, 33, 34, 35]. The electrode spacings are  $L_1 = 1.45 \text{ cm}$ ,  $L_2 = 3.95 \text{ cm}$ ,  $L_3 = 0.79 \text{ cm}$ , and  $L_D = 91.02 \text{ cm}$ . The single-field PEDA voltages and voltage switch time are:  $V_{repeller} = 5000 \text{ V}$ ,  $V_{extractor} = 4600 \text{ V}$ ,  $V_{einzel} = 1728 \text{ V}$ ,

$V_{PEDA1} = 5480 \text{ V}$ , and  $\tau = 2.8 \mu\text{s}$ . These remain the same for the double-field method, with the exceptions of  $V_{PEDA1} = 5510 \text{ V}$  and  $V_{PEDA2} = 2710 \text{ V}$ .

A high mass resolution means that ions with the same  $m/z$  but different  $v_0$  arrive at the detector plane simultaneously. In other words, a smaller  $t_d$  means better mass resolution at that particular  $m/z$ . Figures 2(a) and (b) illustrate this dependence for single- and double-field PEDA. In Figure 2(a), the  $t_d$  for ions between 367 and 438 Da is less than 10 ns over the  $v_0$  range. This is slightly longer than the 3.7 ns decay time of the scintillator, and can therefore be thought of as the effective mass range [36]. According to Figure 2(b), the optimum double-field PEDA mass ranges using the 10 ns threshold are 348-380 Da and 415-480 Da, with excellent resolution over the whole range when a narrower distribution of initial ion velocities is considered. The double-field approach is therefore expected to have a wider overall mass range than the single-field method.

### 3. Methods

Single- and double-field PEDA were experimentally compared using a home-built imaging mass spectrometer optimized for stigmatic microscopy. Time-of-flight mass spectra and ion images were collected for six commercial laser dyes (Auromine O, Rhodamine B, Rhodamine 560 chloride, Rhodamine 640 perchlorate, BBQ, and Exalite 404) and used to establish the mass and spatial resolutions of each technique over the 200-700 Da range. Each dye sample was electrosprayed through a nickel mesh onto conductive 25×25 mm indium tin oxide surfaces and individually placed in a square groove cut into the centre of the

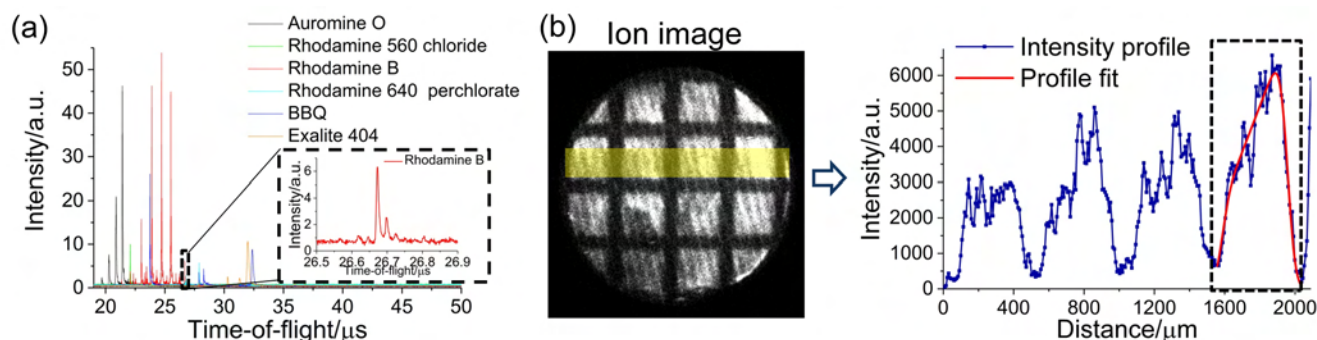


Figure 3: Laser dye mass spectra (a) and ion images (b) are respectively used to characterize the mass and spatial resolution dependence over a 500 Da range of both single- and double-field PEDAs. Mass resolution is determined from the time-of-flight peaks using their full widths at half maximum (FWHM), while spatial resolution is determined using the 20 to 80% intensity rise extracted by fitting (red line) the grid-patterned ion image intensity profiles (blue line).

repeller electrode. This produced gridded dye samples with 67 μm wide gaps and a 498 μm pitch that were used to determine the spatial resolution of the instrument, a process which is illustrated in Figure 3.

Gas-phase ions were desorbed from a 10×10 mm surface spot on each dye sample using defocused 355 nm light incident at 20° (~1-10 mJ/pulse) from a 10 Hz Nd:YAG laser (Continuum Powerlight 8010). The image planes were then electrostatically transferred onto a two-dimensional detector using single- or double-field PEDAs. The former setup uses the five electrode assembly described above (see Figure 1(b)). The einzel lens entrance is a 10 mm thick grounded plate with a removable 2 mm diameter aperture located at the ion velocity focus; it therefore acts as a contrast diaphragm by blocking ions with significant initial velocities transverse to the time-of-flight axis, reducing aberrations in the ion images. The extraction electrode and other einzel lens plates have central iris diameters of 19.5 and 5.0 mm, respectively. The double-field PEDAs optics contain an additional electrode midway between the extractor and einzel lens entrance; its iris is 40 mm in diameter. Under single-field PEDAs conditions, the repeller, extractor, and central einzel lens were set to 5000 V, 4690 V, and 1800 V, respectively. At  $\tau = 2.8 \mu\text{s}$ , the extractor voltage was raised to 5400 V using a fast Behlke switch (HTS 121). In the double-field PEDAs case, the extractor voltage was changed to 4730 V and the new PEDAs lens was set at 2350 V. These electrodes were then raised to 5450 V and 2400 V after a delay of 2.75 μs.

In both cases, ions were detected using a pair of stacked 25 mm microchannel plates (Photonis) coupled with a home-built Exalite 404 scintillator [36]. When compared to typical P47 screens, Exalite 404 scintillators have a faster response time, which allows the mass resolution of the instrument to be more accurately determined. Photons emitted from the scintillator were recorded by a conventional intensified CCD camera (Photonics Science) to create ion images, while time-of-flight spectra were simultaneously recorded using a photomultiplier tube (PMT). Examples of these are presented in Figure 3, and are used in the next section to determine the spatial and mass resolution of each PEDAs technique. It should be noted that the ion images presented here were processed using a centroiding algorithm to enhance the accuracy of the reported spatial resolution.

## 4. Results and discussion

The mass resolution  $R_m$  for each dye peak is determined from its full width at half maximum ( $\Delta t$ ). Using this approach, the resolution is independent of the scintillator decay time [30].

$$R_m = \frac{m}{\Delta m} = \frac{t_f}{2\Delta t} \quad (15)$$

Figures 4(a) and (b) illustrate how mass resolution depends on  $m/z$  for the single- and double-field PEDAs methods, and compares them with simulations modeled using SIMION 8.1 [37]. In these simulations, the initial ion velocity distribution was 500 ms<sup>-1</sup> with a FWHM of 500 ms<sup>-1</sup>, and the emission angle was set normal to the sample surface with FWHM of 60° for both the azimuthal and elevation angles. These values were estimated from existing studies [32, 33, 34, 35] and proved to be a good approximation to reality in previous work using the imaging mass spectrometer described here [31]. In Figure 4, the dashed green lines represents the isotopic limit (i.e.  $\Delta m_{50\%} < 1$  Da). Ion time-of-flights were calibrated with their  $m/z$  using known peaks in the time-of-flight spectra. In each case, the experimental data agrees reasonably well with the SIMION model. The single-field PEDAs optics in Figure 4(a) were focused for ions at 410 Da. The effective mass resolution is centered around this value, with heavier and lighter ions having significantly worse resolution. The range of ions with mass resolutions above 1000  $m/\Delta m$  is roughly 375 to 440 Da. Figure 4(b) illustrates the double-peaked structure indicative of two focused ions. In this example, there are two focused  $m/z$  at 360 and 480 Da, and ions between 330 to 465 Da are mass resolved to at least 1000  $m/\Delta m$ , doubling the range compared to the single-field PEDAs approach.

The key aspect of single-field PEDAs is its ability to preserve image quality while compensating for the initial spread of ion velocities at the sample surface. Therefore, for the enhanced mass range of double-field PEDAs to be advantageous, the technique must similarly maintain spatial resolution. To assess this, the spatial resolution of the ions characterized above were determined from their ion images. Figure 3(b) demonstrates a representative example. A gridded dye sample is initially ionized by the defocused laser and acquired as an ion image with



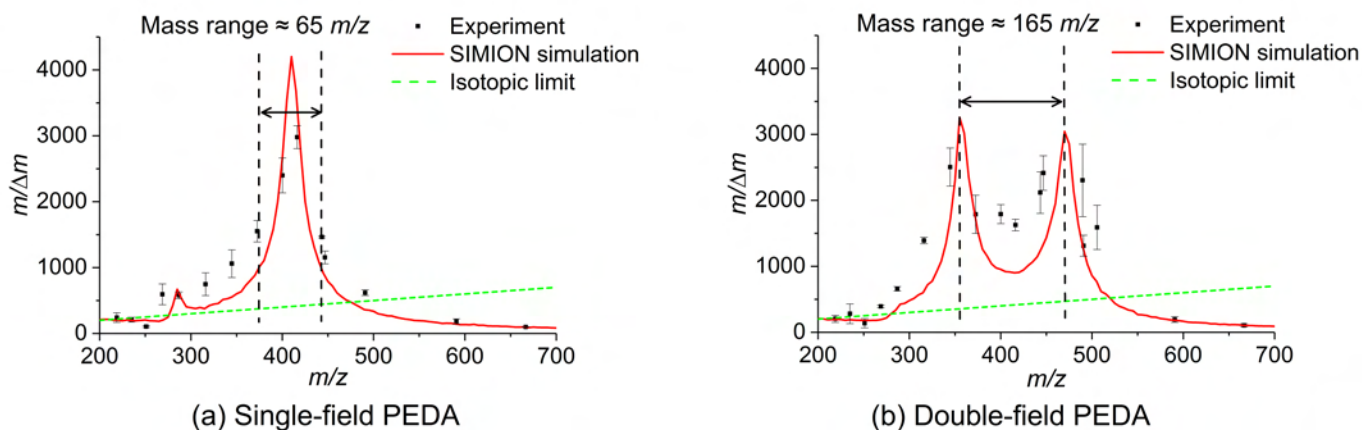


Figure 4: Mass resolution as a function of  $m/z$  for (a) single-field PEDA and (b) double-field PEDA. Experimental results (black squares) are compared with the expected resolution determined by SIMION 8.1 (red line). The double-field method increases the mass range with  $m/\Delta m \geq 1000$  by 100 Da.

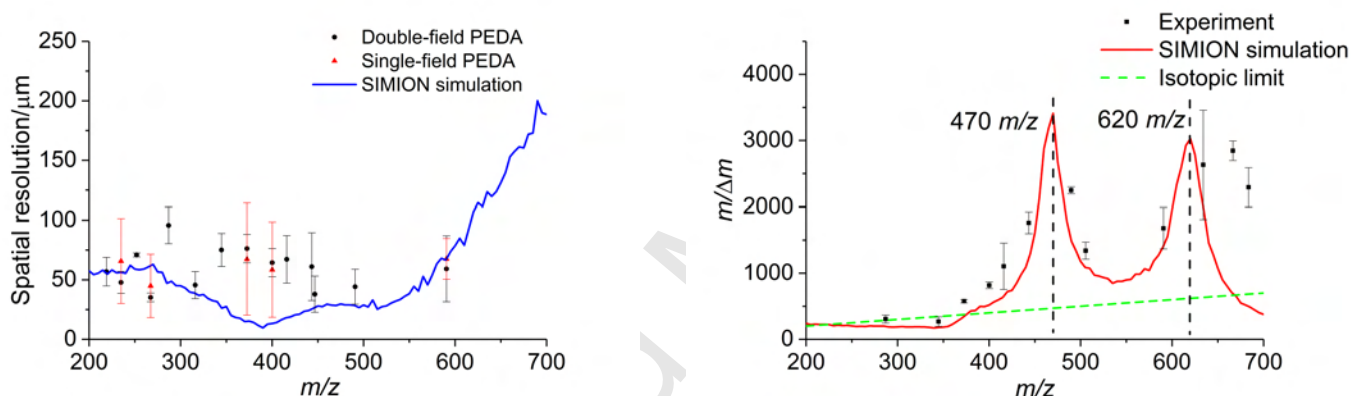


Figure 5: Spatial resolution as a function of  $m/z$  for single-field PEDA (red triangles) and double-field PEDA (black squares). The experimental results are compared with the expected resolution determined by SIMION 8.1 (red line).

Figure 6: Double-field PEDA mass resolution (black squares) as a function of  $m/z$  after being optimized for a higher mass range with the velocity corrected ion extraction method. The experimental results are also compared with the expected resolution determined by SIMION 8.1 (red line).

the CCD camera. An intensity profile is then integrated across the ion image (see the yellow line in Figure 3(b)) to determine the spatial resolution, which is defined as the distance along the profile for which the intensity increases from 20 to 80% of the maximum value [30, 38]. In the present work, the  $20^\circ$  incidence angle of the laser results in sloped rather than rectangular intensity distributions since the fluence of the defocused beam gradually decreases across the sample surface. For this reason, each peak is fit by a Gaussian distribution convoluted with an increasing linear function that represents the incidence angle of the laser. The spatial resolution is then determined by extracting the 20 to 80% rise distance of the convoluted function (ca.  $1.68\sigma$ , where  $\sigma$  is the Gaussian standard deviation) from the average of the fitting results for each intensity profile peak. Figure 5 illustrates the double-field PEDA spatial resolution dependence on  $m/z$  over 200-700 Da. Its spatial resolution is roughly 50  $\mu\text{m}$  over this range. This compares reasonably well with SIMION, which predicts more weakly resolved images outside of the effective mass range, and is essentially identical to the spatial resolution under single-field PEDA conditions [22, 30].

The optimum mass range of single-field PEDA can be tuned using velocity corrected ion extraction [30], where ion optical voltages are simply rescaled to focus ions with different  $m/z$ . This effectively moves the mass resolved PEDA window demonstrated in Figure 4 to different regions of the time-of-flight spectrum. Figure 6 demonstrates that the same method can also be applied to double-field PEDA. In this example, the peaks previously observed at 355 and 470 Da were shifted to 470 and 620 Da by multiplying the ion optics voltages by a factor of 1.3. As a result, the mass range of double-field PEDA where the mass resolution remains above 1000  $m/\Delta m$  is optimized for larger  $m/z$ .

## 5. Conclusions

Simultaneously focusing two  $m/z$  allows microscope MSI to be performed over a mass range that is roughly double what can be achieved using single-field PEDA. For the home-built mass spectrometer described here, the mass ranges where  $m/\Delta m \geq$

1000 were 65 and 165 Da, respectively, for single-field PEDAS<sup>370</sup>  
at 410 Da and double-field PEDAS at 360 and 480 Da. This was<sup>371</sup>  
accomplished without any comparative loss in the spatial res-<sup>372</sup>  
olution or quality of the associated ion images. The broader,<sup>373</sup>  
mass range of double-field PEDAS also extends to velocity cor-<sup>374</sup>  
rected ion extraction, which has the benefit of allowing large<sup>375</sup>  
mass ranges to be sampled and imaged more quickly. More<sup>376</sup>  
generally, this points to the fact that the temporal focusing of<sup>377</sup>  
many ions, either through time-variant pulses or multi-electrode<sup>378</sup>  
systems, will likely play a key role in the push to maximize the<sup>379</sup>  
mass range of microscope MSI while preserving effective mass,<sup>380</sup>  
and spatial resolutions.<sup>381</sup>

## 6. Acknowledgments

The authors gratefully acknowledge the UK EPSRC (Pro-  
gramme Grant Nos. EP/G00224X/1 and EP/L005913/1) and  
the EU (FP7 ITN 'ICONIC', Project No. 238671) for their sup-  
port. A.G. also thanks the China Scholarship Council (CSC)  
for their generous backing.

## 7. References

- [1] M. L. Pacholski, N. Winograd, Imaging with mass spectrometry, *Chemical Reviews* 99 (1999) 2977–3005.
- [2] L. A. McDonnell, R. Heeren, Imaging mass spectrometry, *Mass Spectrometry Reviews* 26 (2007) 606–643.
- [3] E. R. Amstalden van Hove, D. F. Smith, R. M. A. Heeren, A concise review of mass spectrometry imaging, *Journal of Chromatography A* 1217 (2010) 3946–3954.
- [4] R. M. Caprioli, T. B. Farmer, J. Gile, Molecular imaging of biological samples: localization of peptides and proteins using MALDI-TOF MS, *Analytical Chemistry* 69 (1997) 4751–4760.
- [5] M. Karas, D. Bachmann, U. Bahr, F. Hillenkamp, Matrix-assisted ultraviolet laser desorption of non-volatile compounds, *International Journal of Mass Spectrometry and Ion Processes* 78 (1987) 53–68.
- [6] A. Benninghoven, W. Siewertmann, Detection, identification, and structural investigation of biologically important compounds by secondary ion mass spectrometry, *Analytical Chemistry* 50 (1978) 1180–1184.
- [7] Z. Takats, J. M. Wiseman, B. Gologan, R. G. Cooks, Mass spectrometry sampling under ambient conditions with desorption electrospray ionization, *Science* 306 (2004) 471–473.
- [8] J. McMahon, N. Dookeran, P. Todd, Organic ion imaging beyond the limit of static secondary ion mass spectrometry, *Journal of the American Society for Mass Spectrometry* 6 (1995) 1047–1058.
- [9] P. Chaurand, M. E. Sanders, R. A. Jensen, R. M. Caprioli, Proteomics in diagnostic pathology: profiling and imaging proteins directly in tissue sections, *The American Journal of Pathology* 165 (2004) 1057–1068.
- [10] S. S. Rubakhin, J. C. Jurchen, E. B. Monroe, J. V. Sweedler, Imaging mass spectrometry: fundamentals and applications to drug discovery, *Drug Discovery Today* 10 (2005) 823–837.
- [11] M. R. Groseclose, M. Andersson, W. M. Hardesty, R. M. Caprioli, Identification of proteins directly from tissue: *in situ* tryptic digestions coupled with imaging mass spectrometry, *Journal of Mass Spectrometry* 42 (2007) 254–262.
- [12] M. Stoeckli, D. Staab, A. Schweitzer, Compound and metabolite distribution measured by MALDI mass spectrometric imaging in whole-body tissue sections, *International Journal of Mass Spectrometry* 260 (2007) 195–202.
- [13] Y. Sugiura, M. Setou, Imaging mass spectrometry for visualization of drug and endogenous metabolite distribution: toward *in situ* pharmacometabolomes, *Journal of Neuroimmune Pharmacology* 5 (2010) 31–43.
- [14] T. Nagatani, S. Saito, Development of an ultra high resolution scanning electron microscope by means of a field emission source and in-lens system, *Scanning Microscopy* 1 (1987) 901–909.

- [15] B. Schueler, P. Sander, D. A. Reed, A time-of-flight secondary ion microscope, *Vacuum* 41 (1990) 1661–1664.
- [16] B. W. Schueler, Microscope imaging by time-of-flight secondary ion mass spectrometry, *Microscopy Microanalysis Microstructures* 3 (1992) 119–139.
- [17] R. W. Odom, Secondary ion mass spectrometry imaging, *Applied Spectroscopy Reviews* 29 (1994) 67–116.
- [18] G. H. Morrison, G. Slodzian, Ion microscopy, *Analytical Chemistry* 47 (1975) 932A–943A.
- [19] X. Llopart, R. Ballabriga, M. Campbell, L. Tlustos, W. Wong, Timepix, a 65k programmable pixel readout chip for arrival time, energy and/or photon counting measurements, *Nuclear Instruments and Methods in Physics Research, Section A: Accelerators, Spectrometers, Detectors and Associated Equipment* 581 (2007) 485–494.
- [20] A. Nomerotski, S. Adigun-Boaye, M. Brouard, E. Campbell, A. Clark, J. Crooks, J. J. John, A. J. Johnsen, C. Slater, R. Turchetta, C. Vallance, E. Wilman, W. H. Yuen, Pixel imaging mass spectrometry with fast silicon detectors, *Nuclear Instruments and Methods in Physics Research Section A: Accelerators, Spectrometers, Detectors and Associated Equipment* 633 (2011) S243–S246.
- [21] J. J. John, M. Brouard, A. Clark, J. Crooks, E. Halford, L. Hill, J. W. L. Lee, A. Nomerotski, R. Pisarczyk, I. Sedgwick, PimMS, a fast event-triggered monolithic pixel detector with storage of multiple timestamps, *Journal of Instrumentation* 7 (2012) C08001.
- [22] M. Brouard, E. Halford, A. Lauer, C. S. Slater, B. Winter, W. Yuen, J. J. John, L. Hill, A. Nomerotski, A. Clark, J. Crooks, I. Sedgwick, R. Turchetta, J. W. L. Lee, C. Vallance, E. Wilman, The application of the fast, multi-hit, pixel imaging mass spectrometry sensor to spatial imaging mass spectrometry, *Review of Scientific Instruments* 83 (2012) 114101.
- [23] C. Vallance, M. Brouard, A. Lauer, C. S. Slater, E. Halford, B. Winter, S. J. King, J. W. L. Lee, D. E. Pooley, I. Sedgwick, R. Turchetta, A. Nomerotski, J. J. John, L. Hill, Fast sensors for time-of-flight imaging applications, *Physical Chemistry Chemical Physics* 16 (2014) 383–395.
- [24] A. T. Clark, J. P. Crooks, I. Sedgwick, R. Turchetta, J. W. L. Lee, J. J. John, E. S. Wilman, L. Hill, E. Halford, C. S. Slater, B. S. Winter, W. H. Yuen, S. H. Gardiner, M. L. Lipciuc, M. Brouard, A. Nomerotski, C. Vallance, Multimass velocity-map imaging with the pixel imaging mass spectrometry (PimMS) sensor: an ultra-fast event-triggered camera for particle imaging, *The Journal of Physical Chemistry A* 116 (2012) 10897–10903.
- [25] W. C. Wiley, I. H. McLaren, Time-of-Flight Mass Spectrometer with Improved Resolution, *Review of Scientific Instruments* 26 (1955) 1150–1157.
- [26] S. M. Colby, T. B. King, J. P. Reilly, Improving the resolution of matrix-assisted laser desorption/ionization time-of-flight mass spectrometry by exploiting the correlation between ion position and velocity, *Rapid Communications in Mass Spectrometry* 8 (1994) 865–868.
- [27] R. S. Brown, J. J. Lennon, Mass resolution improvement by incorporation of pulsed ion extraction in a matrix-assisted laser desorption/ionization linear time-of-flight mass spectrometer, *Analytical Chemistry* 67 (1995) 1998–2003.
- [28] M. L. Vestal, P. Juhasz, S. A. Martin, Delayed extraction matrix-assisted laser desorption time-of-flight mass spectrometry, *Rapid Communications in Mass Spectrometry* 9 (1995) 1044–1050.
- [29] J. Aoki, H. Hazama, M. Toyoda, Novel ion extraction method for imaging mass spectrometry, *Journal of the Mass Spectrometry Society of Japan* 59 (2011) 57–61.
- [30] B. Winter, E. Halford, M. Brouard, Velocity corrected ion extraction in microscope mode imaging mass spectrometry, *International Journal of Mass Spectrometry* 356 (2013) 14–23.
- [31] E. Halford, B. Winter, M. Mills, S. Thompson, V. Parr, J. John, A. Nomerotski, C. Vallance, R. Turchetta, M. Brouard, Modifications to a commercially available linear mass spectrometer for mass-resolved microscopy with the pixel imaging mass spectrometry (PimMS) camera, *Rapid Communications in Mass Spectrometry* 28 (2014) 1649–1657.
- [32] R. C. Beavis, B. T. Chait, Velocity distributions of intact high mass polypeptide molecule ions produced by matrix assisted laser desorption, *Chemical Physics Letters* 181 (1991) 479–484.
- [33] W. Zhang, B. T. Chait, Radial velocity distributions of molecular ions produced by matrix-assisted laser desorption/ionization, *International Journal of Mass Spectrometry and Ion Processes* 160 (1997) 259–267.

- 441 [34] M. Glückmann, M. Karas, The initial ion velocity and its dependence on  
442 matrix, analyte and preparation method in ultraviolet matrix-assisted laser  
443 desorption/ionization, *Journal of Mass Spectrometry* 34 (1999) 467–477.
- 444 [35] C.-W. Liang, C.-H. Lee, Y.-T. Lee, C.-K. Ni, Plume expansion dynam-  
445 ics of matrix-assisted laser desorption ionization, *Chemistry–An Asian*  
446 *Journal* 6 (2011) 2986–2991.
- 447 [36] B. Winter, S. King, M. Brouard, C. Vallance, A fast microchannel plate-  
448 scintillator detector for velocity map imaging and imaging mass spec-  
449 trometry, *Review of Scientific Instruments* 85 (2014) 023306.
- 450 [37] D. J. Manura, D. A. Dahl, SIMION Version 8.0/8.1 User Manual, Scien-  
451 tific Instrument Services, Inc., 2011.
- 452 [38] T. L. Colliver, C. L. Brummel, M. L. Pacholski, F. D. Swanek, A. G.  
453 Ewing, N. Winograd, Atomic and molecular imaging at the single-cell  
454 level with TOF-SIMS, *Analytical Chemistry* 69 (1997) 2225–2231.



**Mass-resolved ion microscope imaging over expanded mass ranges using double-field post-extraction differential acceleration**

Ang Guo, Michael Burt, Mark Brouard

**Highlights**

- A stigmatic ion imaging technique employing two pulsed electrodes is presented.
- Two  $m/z$  distributions are simultaneously focused; enlarging the resolved  $m/z$  range.
- The effective mass range is increased without any reduction in ion image quality.

